

Supporting Information

Ultrahigh Solar Steam Generation Rate of a Vertically Aligned Reduced Graphene Oxide Foam Realized by Dynamic Compression

Wei Li,^{1,2} Xiaohan Tian,¹ Xiaofeng Li,^{1,*} Shuang Han,² Changjun Li,² Xian-Zhi Zhai,¹ Yu Kang³ and Zhong-Zhen Yu^{2,*}

¹ State Key Laboratory of Organic-Inorganic Composites, College of Materials Science and Engineering, Beijing University of Chemical Technology, Beijing 100029, China

² Beijing Key Laboratory of Advanced Functional Polymer Composites, Beijing University of Chemical Technology, Beijing 100029, China

³ Analysis and Test Center, Beijing University of Chemical Technology, Beijing 100029, China

*E-mail: xfli@mail.buct.edu.cn (X. Li); yuzz@mail.buct.edu.cn (Z.-Z. Yu)

Heat localization behaviour of V-RGO foam with a compressive strain of 47.1% under 1 sun irradiation:

The conductive heat flux from the top evaporation surface of the foam to the bulk water (J_{cond}) can be calculated using eq. S1:¹

$$J_{\text{cond}} = \kappa (\Delta T/L) \quad (\text{S1})$$

Where κ is the thermal conductivity of the V-RGO foam, which is $\sim 3.2 \text{ mW m}^{-1} \text{ K}^{-1}$. $\Delta T/L$ represents the temperature gradient along the vertical axis of the V-RGO foam ($\sim 420 \text{ K m}^{-1}$). Thus, J_{cond} is approximately 1.34 W m^{-2} .

The conductive heat loss (E_{cond}) can be calculated with eq. S2:¹

$$E_{\text{cond}} = J_{\text{cond}} \times A \quad (\text{S2})$$

where A is the cross-sectional area of the conductive path ($1.62 \times 10^{-4} \text{ m}^2$). Thus, E_{cond} is approximately $2.18 \times 10^{-4} \text{ W}$, which can be negligible.

The conductive loss efficiency (η_{cond}) is calculated with eq. S3:²

$$\eta_{\text{cond}} = J_{\text{cond}}/J_{\text{in}} \quad (\text{S3})$$

where J_{in} is the energy put into the system (1 kW m^{-2}). Thus, η_{cond} is 0.13%. Compared to convection and radiation losses, the conductive heat loss can be ignored.³

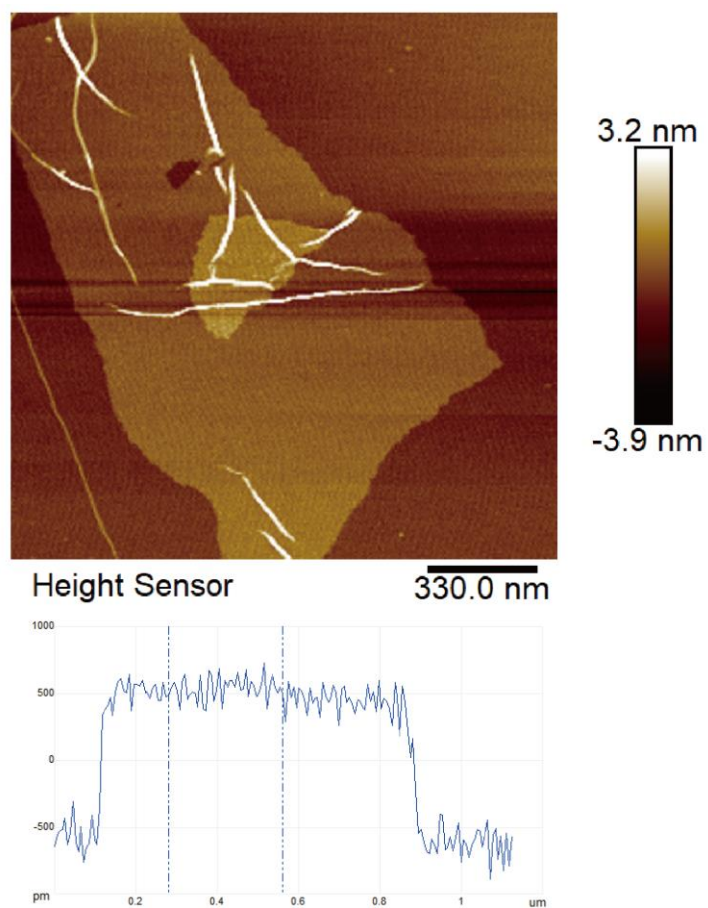


Figure S1. AFM image of GO sheet.

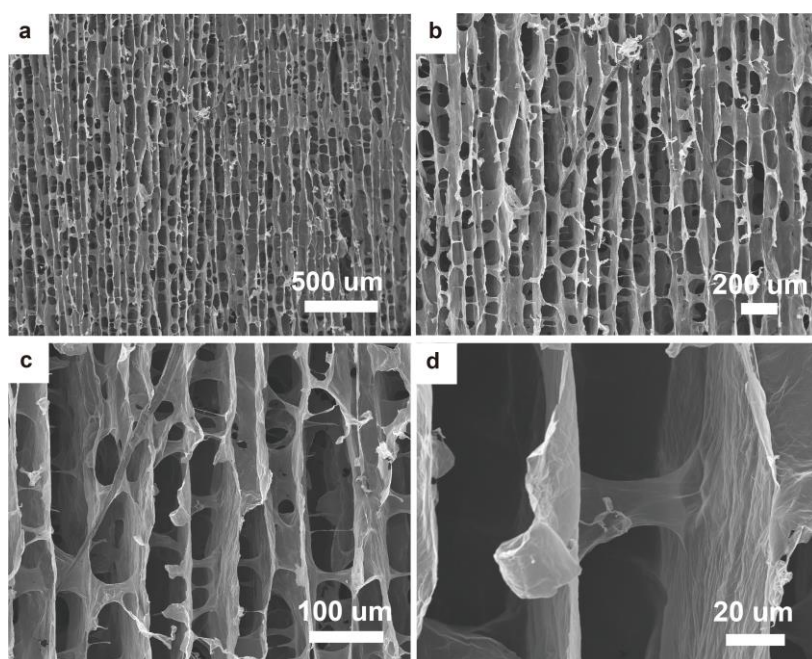


Figure S2. (a-d) SEM images of V-RGO foam at different magnifications.

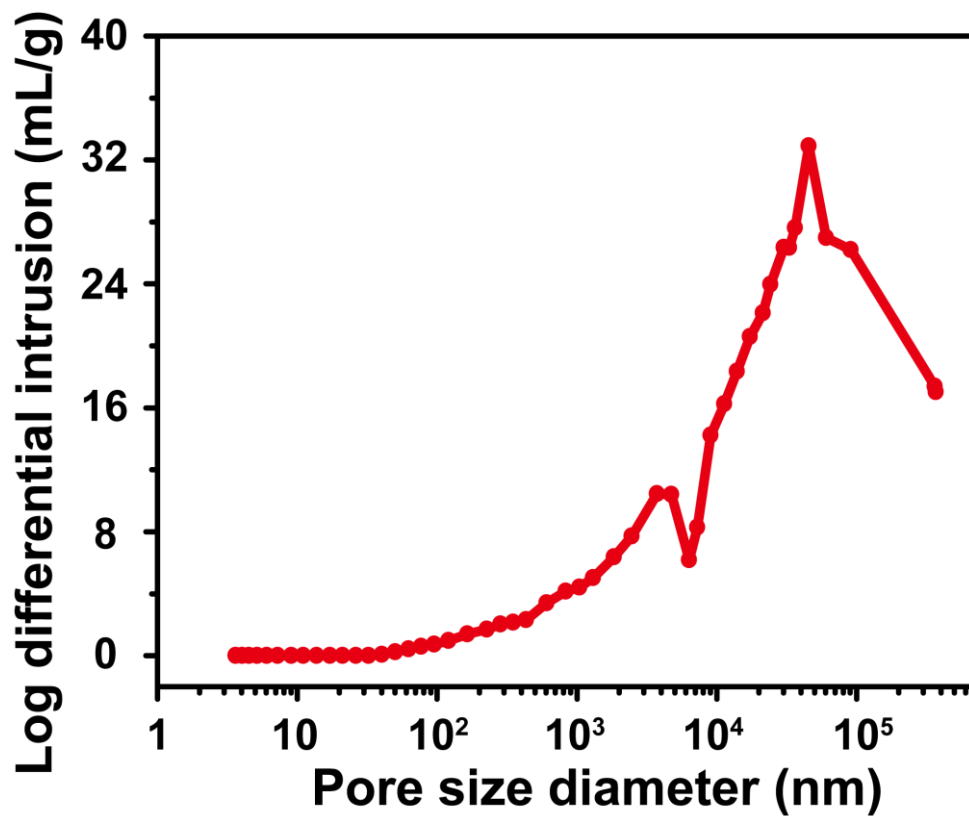


Figure S3. Pore size distribution of V-RGO foam calculated by a mercury intrusion porosimetry method.



Figure S4. Rapid water absorption of V-RGO foam.

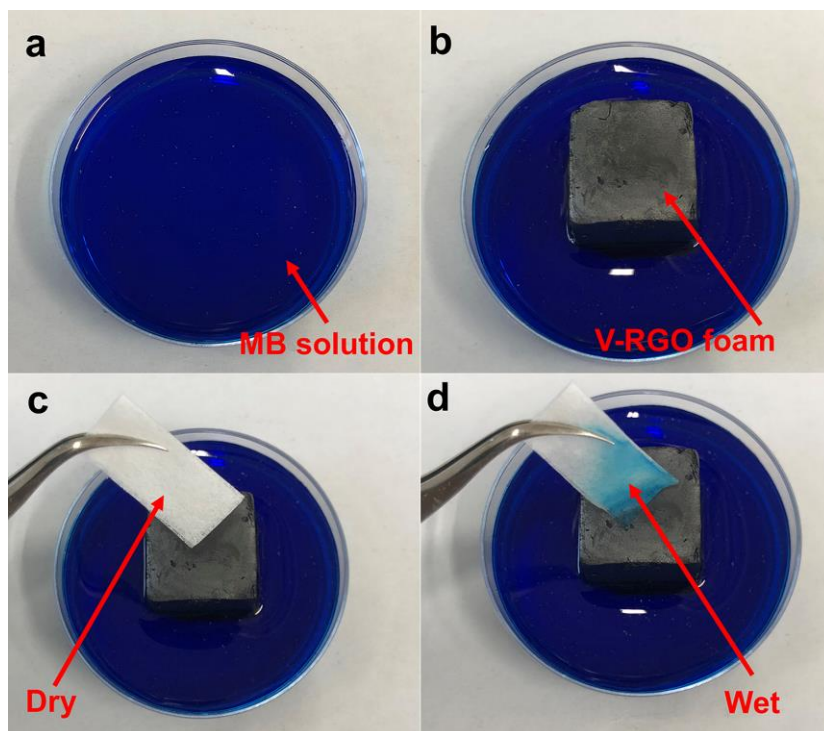


Figure S5. (a) Aqueous solution of methylene blue (MB) with a concentration of 50 ppm. (b) Water wettability of the V-RGO foam indicates its hydrophilicity. (c, d) When a dry paper touches the top surface of the V-RGO foam, it could be dyed and wetted quickly and absorb water from the foam.

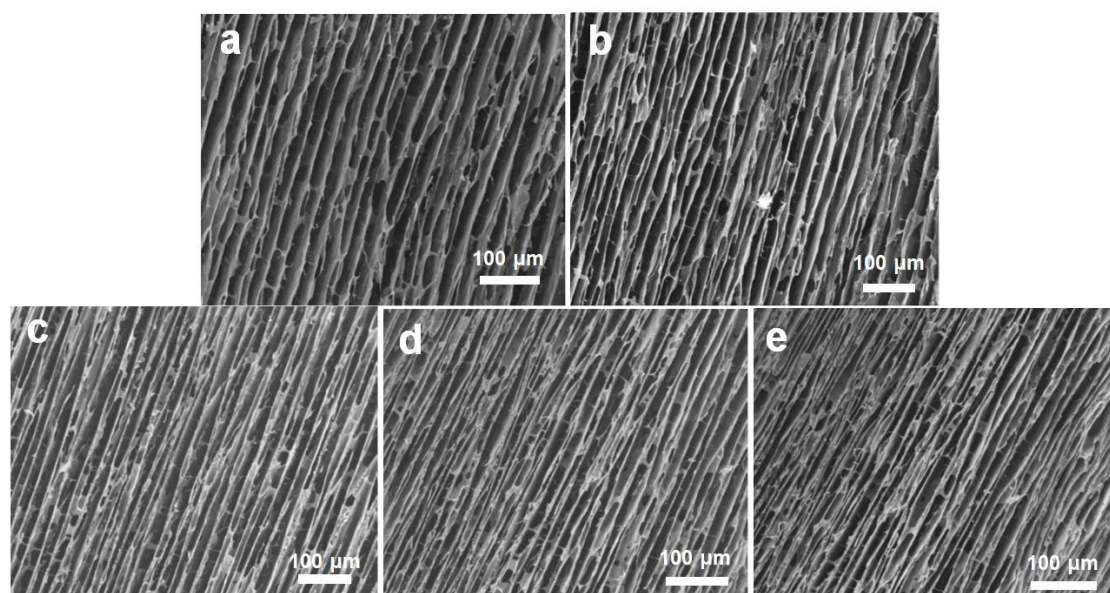


Figure S6. SEM images of cross-sections of freeze-dried V-RGO foam compressed at the stains of (a) 11.8%, (b) 23.5%, (c) 35.3%, (d) 52.9%, and (e) 58.9%.

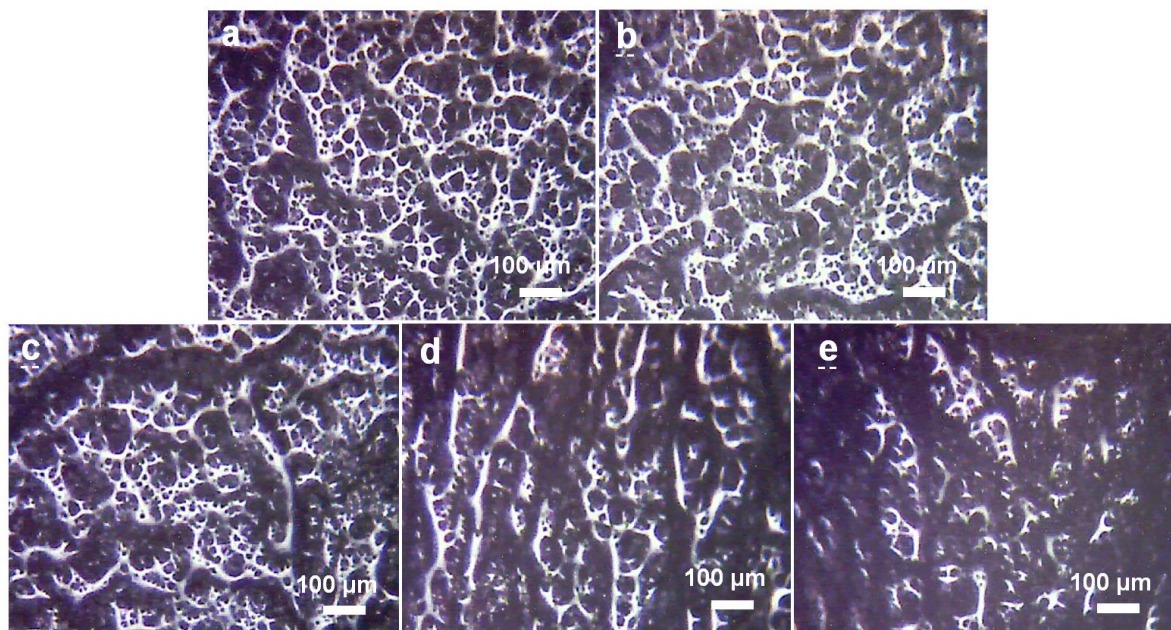


Figure S7. Optical images of the surfaces of the V-RGO foams compressed at strains of (a) 11.8%, (b) 23.5%, (c) 35.3%, (d) 52.9%, and (e) 58.9%.

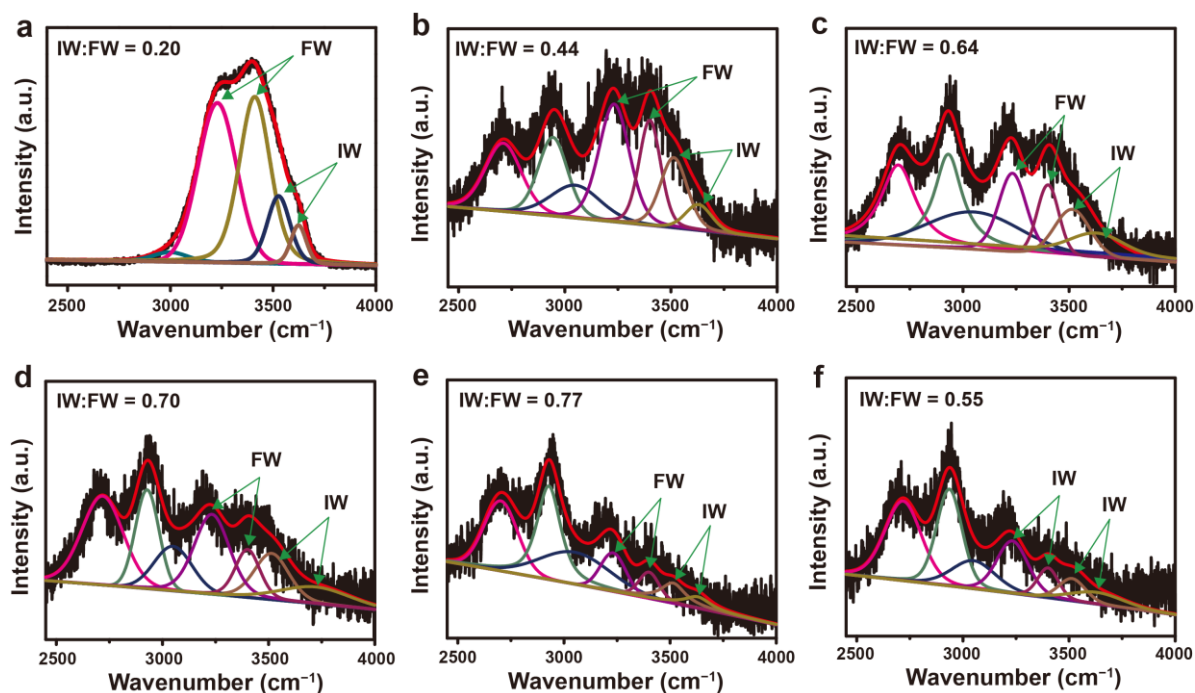


Figure S8. Fitting curves of the energy region of O–H stretching mode in the Raman spectra of (a) pure water, and the water in the V-RGO foams with different compressive strains of (b) 11.8%, (c) 23.5%, (d) 35.3%, (e) 52.9%, and (f) 58.9%.

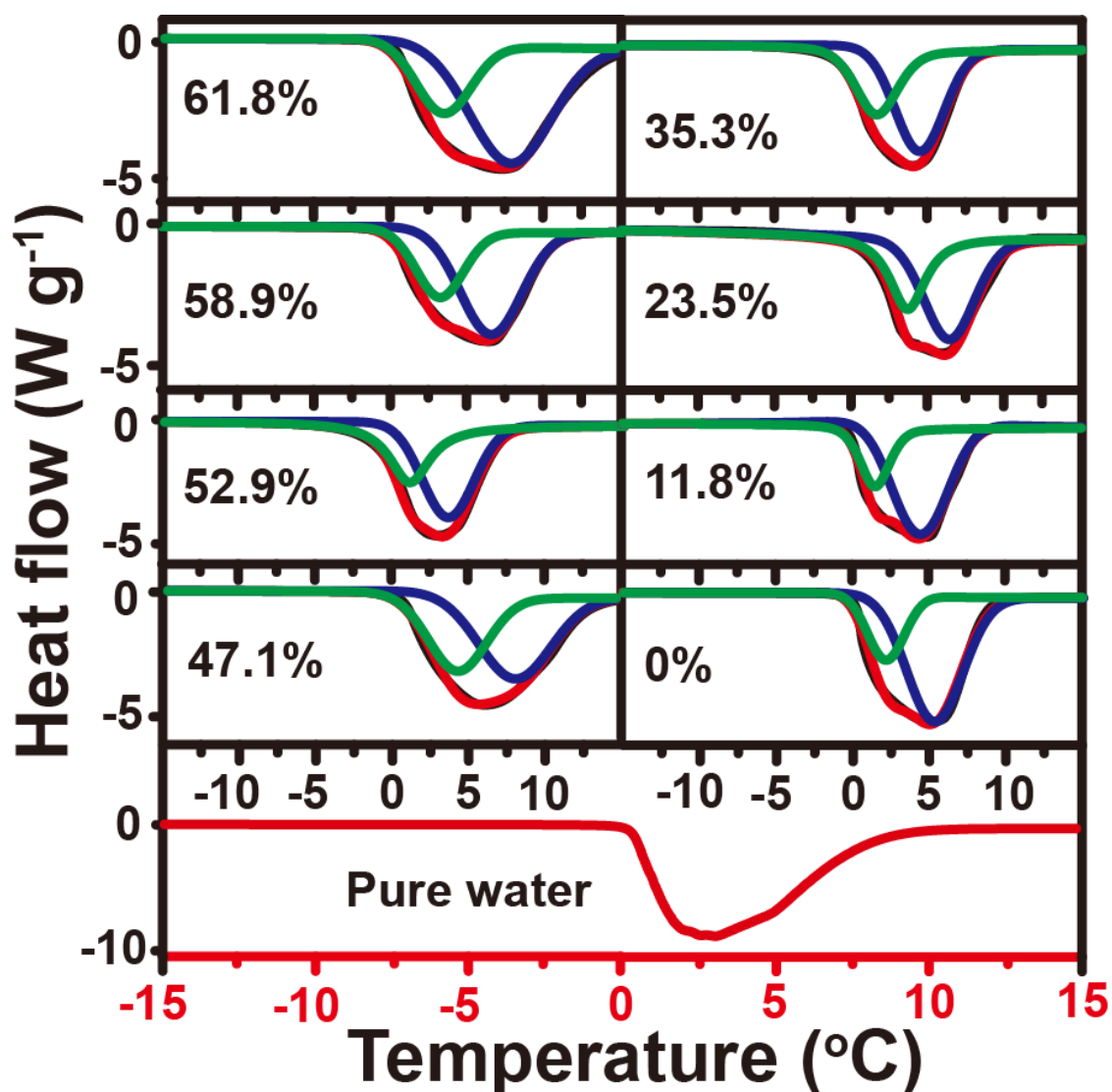


Figure S9. Fitting curves of the melting behavior of ice and water frozen in V-RGO with compressive strains of 0%, 11.8%, 23.5%, 35.3%, 47.1%, 52.9%, 58.9% and 61.8%. On the basis of the method reported by Yu et al,⁴ the fractions of free water, intermediate water, and bound water in V-RGO foams with compressive strains are measured by DSC. **Figure S9** shows the fitted curves of the melting behaviors of water frozen in V-RGO foams, which are used for estimating the fractions of three types of water (**Table S1**).

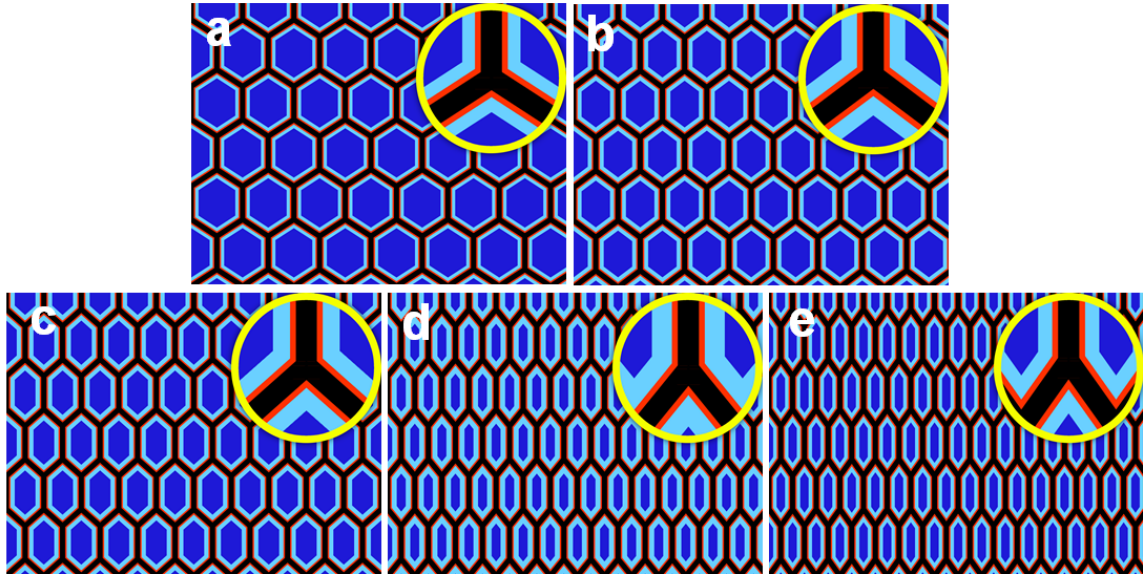


Figure S10. Schematic illustrating the three types of water in the V-RGO foam with compressive strains of (a) 11.8%, (b) 23.5%, (c) 35.3%, (d) 52.9%, and (e) 58.9%, where FW, IW and BW represent free water (blue), intermediate water (light blue), and bound water (red), respectively.

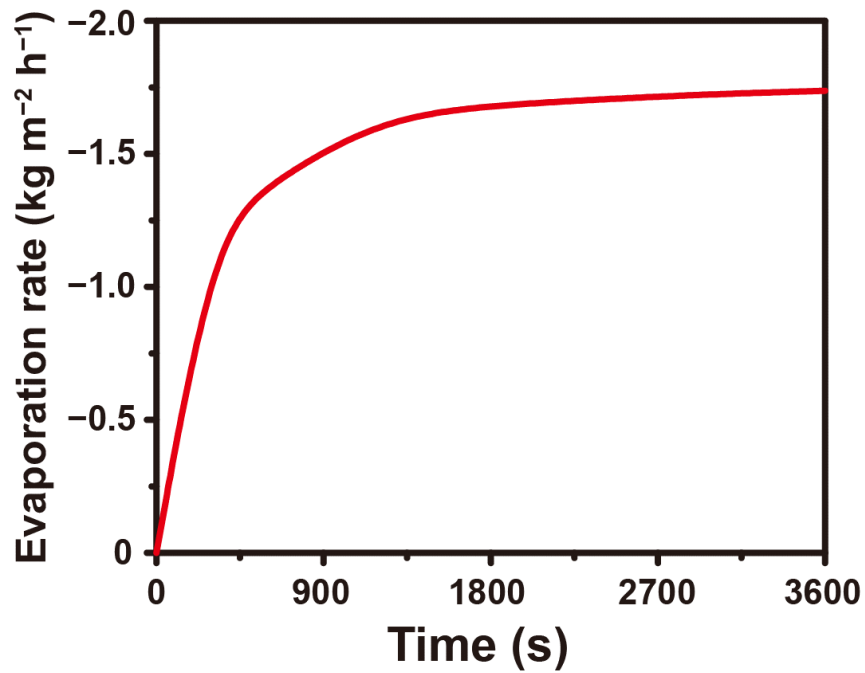


Figure S11. Plot of water evaporation rate versus time for RGO foam under 1-sun irradiation.

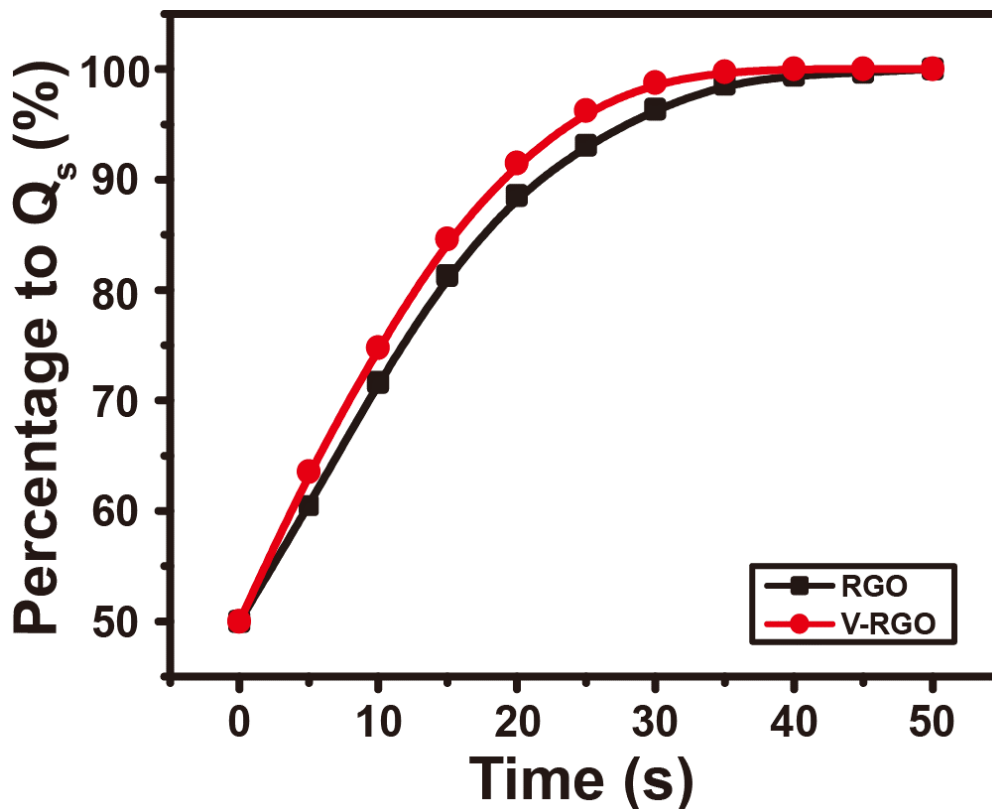


Figure S12. Percentages to saturated water content (Q_s) of RGO and V-RGO foams as a function of time. The transport of water in the foam channels is achieved by capillary pumping, and the diffusion of water in the molecular grids is enabled by the osmotic effect. Therefore, water transport in the foam is evaluated by the dynamic analysis of swelling of the foam network. In the design of water absorption experiment, Q_s represents the water content of the foam after saturation. We use a bibulous paper with strong capillary, to absorb the water from the molecular meshes and micron channels in the saturated foam, and carefully control the water content in the foam down to half of the original value ($0.5 Q_s$), realizing a half-saturated state. The swollen time from the half-saturated state to the saturated state reveals the water transport behavior in the foam.

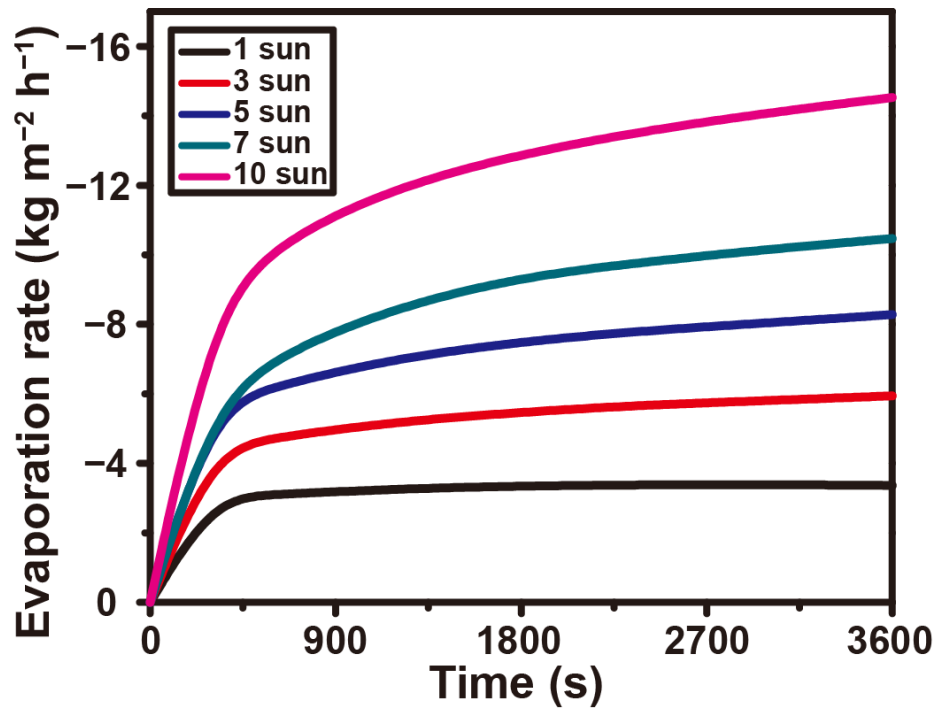


Figure S13. Water evaporation rates of the V-RGO foam with a compressive strain of 47.1% under 1, 3, 5, 7, and 10-sun irradiation.

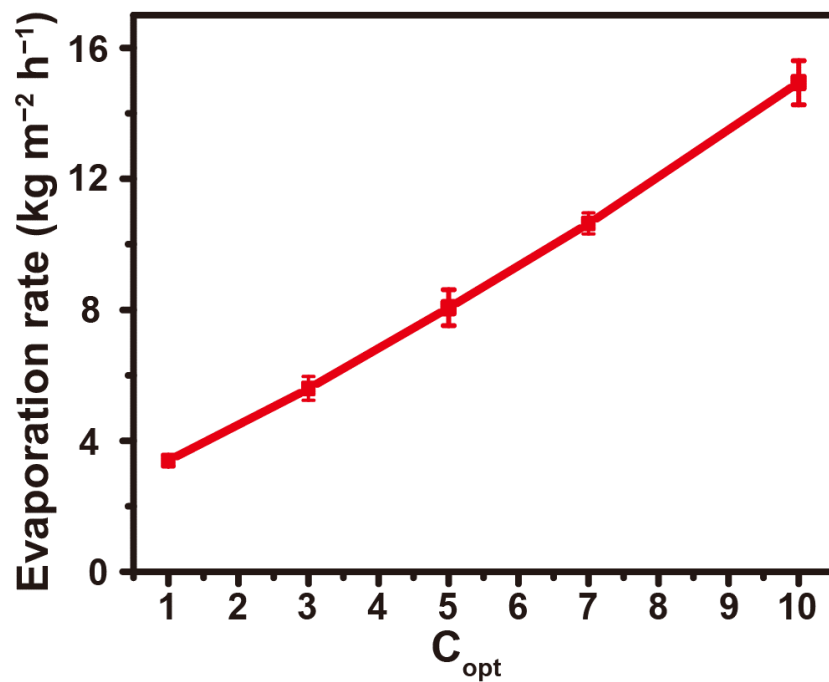


Figure S14. Solar steam generation rates of V-RGO foam with a compressive strain of 47.1% under 1, 3, 5, 7 and 10-sun irradiation.

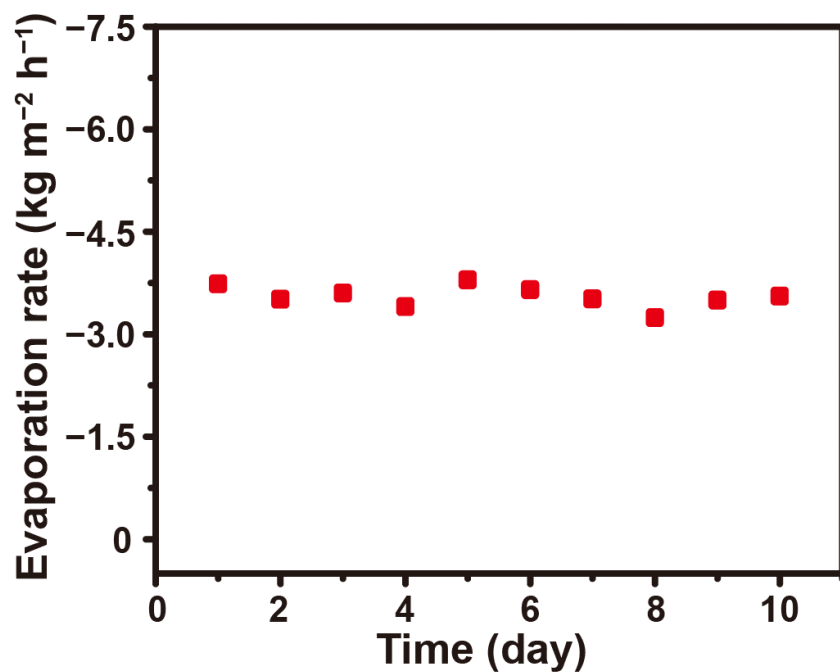


Figure S15. Water evaporation rates of V-RGO foam with a compressive strain of 47.1% under 1-sun irradiation for 10 consecutive days (10 h/day).

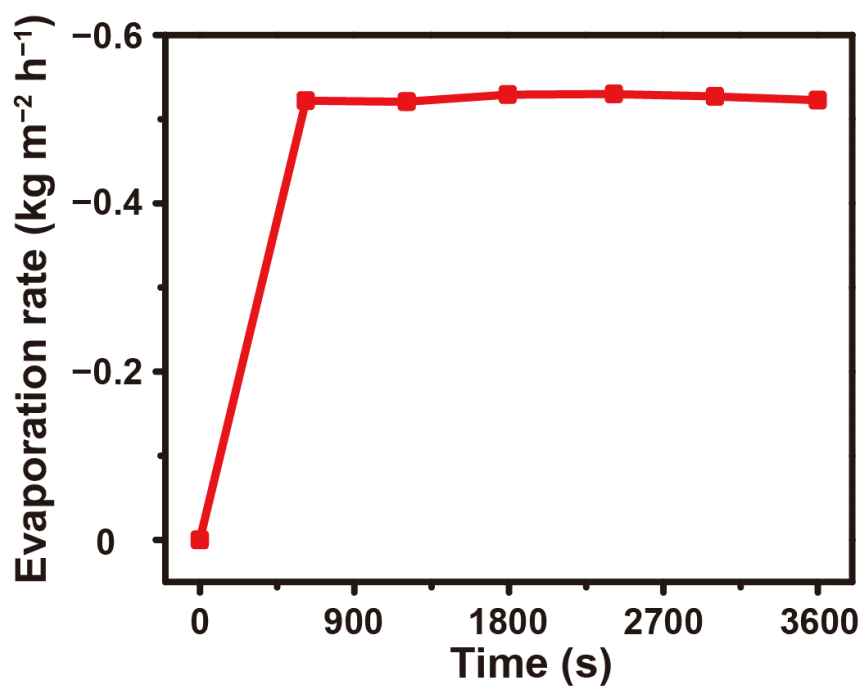


Figure S16. Water evaporation rates of V-RGO foam with a compressive strain of 47.1% in dark.

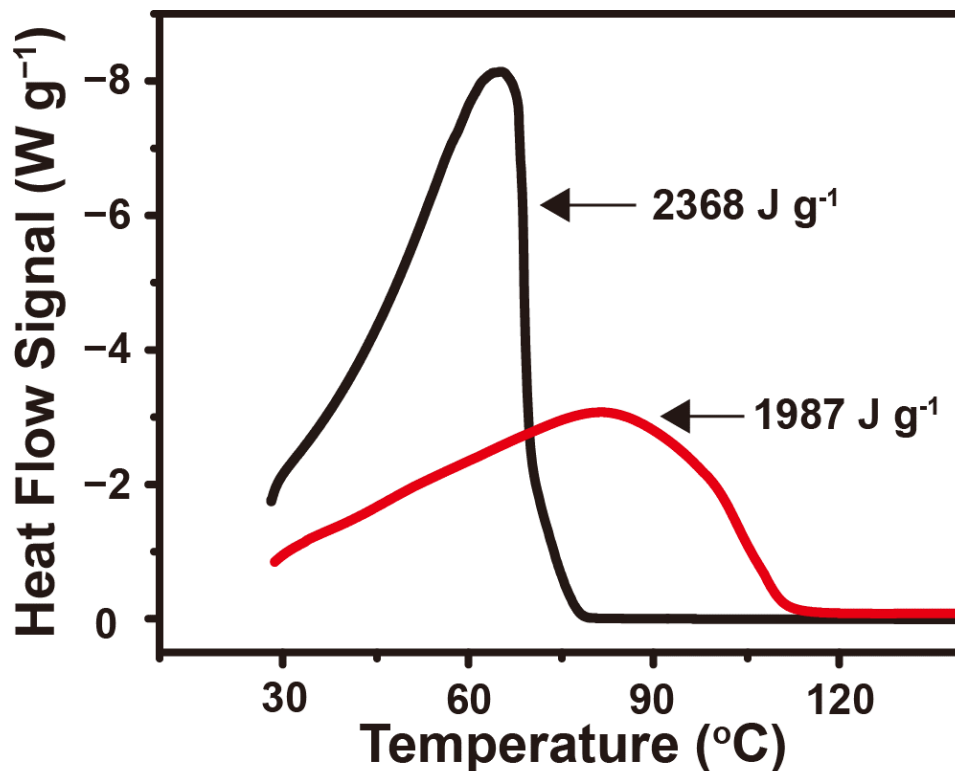


Figure S17. DSC curves of pure water and V-RGO foam. To measure the vaporization enthalpy, the foam filled with water is placed in an open aluminum crucible and measured at a temperature range from 30 to 135 °C under a nitrogen atmosphere (20 mL min⁻¹) with a heating rate of 5 K min⁻¹. DSC experiments exhibit a reduced vaporization enthalpy (1987 J g⁻¹) over V-RGO foam compared with that of free evaporation water (2368 J g⁻¹), which is similar to previous report.⁵ Note that the actual evaporation process is a slight dehydration process, while the DSC measurement is a complete dehydration process. So, the enthalpy calculated on the basis of the DSC curves cannot be directly used for calculating the solar-thermal energy conversion efficiency.⁶

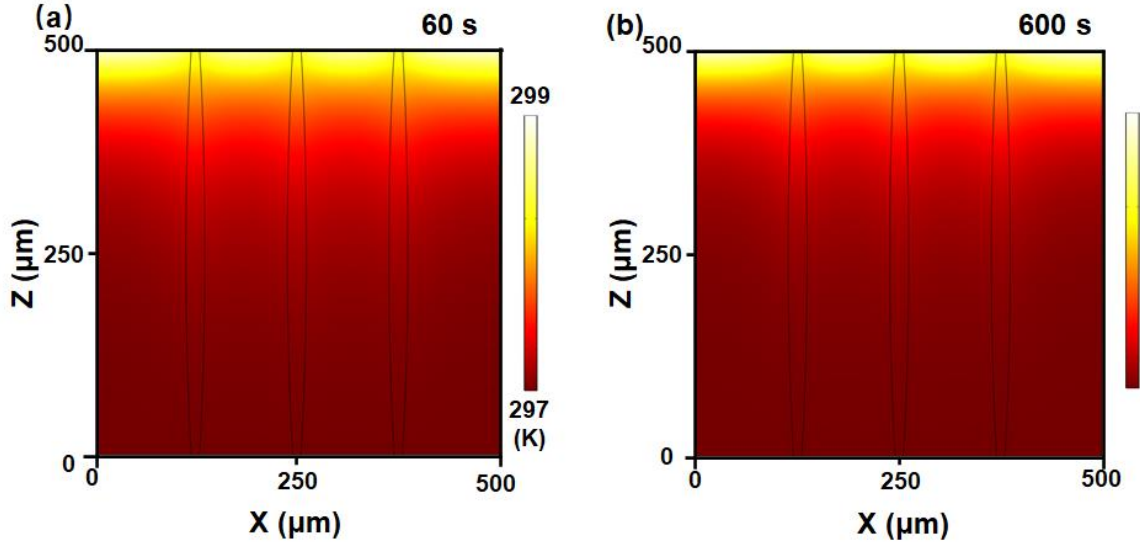


Figure S18. Transient state simulations of temperature distributions at (a) 60 s and (b) 600 s.

On the basis of the constraint of water in the RGO network and the convection in the vertical channels, the heat transfer in the V-RGO foam can be described by eq. S4:⁷

$$E_{in} = \rho C_p \frac{\partial T(x,t)}{\partial t} + \rho C_p v \cdot \nabla T(x, t) + \nabla [k \nabla T(x, t)] \quad (S4)$$

Where E_{in} is the thermal energy input from the solar-thermal energy conversion; x is the space vector; and t is time; ρ is the mass density; C_p is the liquid thermal capacity; $T(x, t)$ is the local temperature; v and k are the fluid flow speed and the thermal conductivity of water medium, respectively. As reported, the heat transfer model can be simplified as a semi-infinite medium for the Cartesian coordinate system.⁸ We use a COMSOL Multiphysics 4.4 software to simulate the temperature distribution under the steady and transient analysis mode. The 2D model is discretized into 1000 elements. A constant heat flux density of 0.1 kW m^{-2} appears on the top ($Z = 500 \text{ } \mu\text{m}$), which corresponds to the solar energy input on the surface of V-RGO foam, and the energy consumption used for evaporation is about 0.9 kW m^{-2} . The balanced heat flux is 0.1 kW m^{-2} . The temperature distributions under the steady and transient analysis mode at (a) 60 s and (b) 600 s are shown in **Figure S18**.

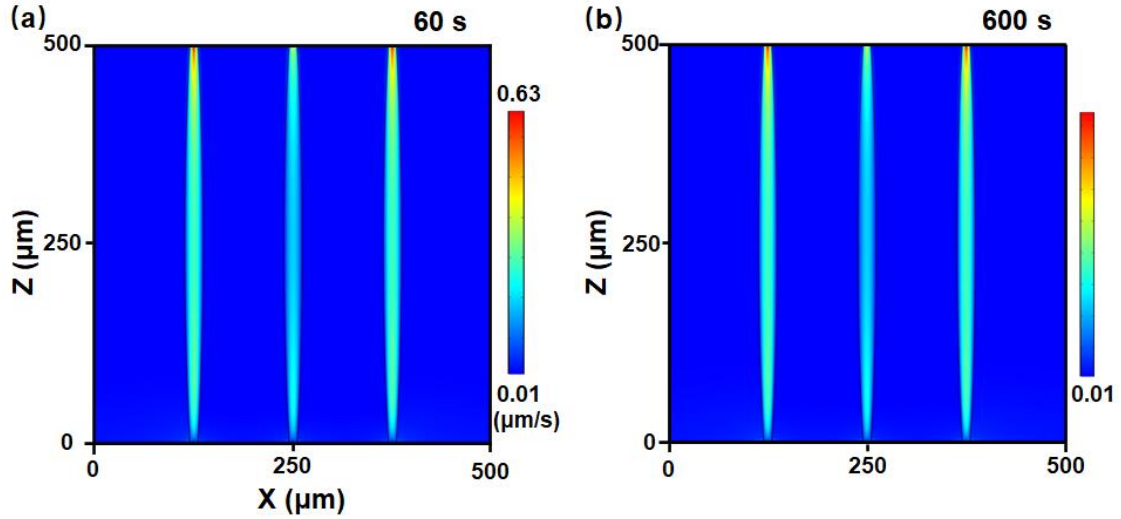


Figure S19. Steady state simulation of water transport caused by the water losses from the evaporation surface of the foam under 1-sun irradiation at (a) 60 s, and (b) 600 s. We established a water transport steady state model on the basis of the biphasic mixture theory to simulate the water transport behavior in the foam, which considers the flow of a fluid through a porous medium with different porosities and ignores the complexity caused by deformation. The RGO network and permeable fluid are regarded as permeable solids and fluids respectively.⁹ The mass conservation for water phase in the foam is described by eq. S5:¹⁰

$$\nabla \cdot v_p = \nabla \cdot [\phi_w \cdot (v_p - v_w)] \quad (\text{S5})$$

where ϕ_w , v_p , and v_w are the water volume fraction, intrinsic velocity of carbon-based material, and intrinsic velocity of water phase, respectively. In addition, the momentum conservations of carbon-based material and liquid phase are determined by eqs. S6 and S7:¹¹

$$\nabla \cdot \sigma_p + f_{pw} (v_w - v_p) = 0 \quad (\text{S6})$$

$$\phi_w \nabla \cdot P + \sum f_{iw} (v_w - v_i) = 0 \quad (\text{S7})$$

Where σ_p and f represent the stress tensor and drag force between the two phases; P is the intrinsic fluid pressure, including the remaining part of internal fluid pressure and the osmotic pressure. Based on the experimental data, the predetermined v_{w0} is set on the top boundary of the RGO skeleton. In the steady-state analysis mode, COMSOL multiphysics 4.4 is used for

numerical simulations. The 2D model is discretized into 1000 elements. For qualitative analysis, we assume $f_{wp} = 10^{12} \text{ N s m}^{-2}$ in the RGO network to simplify the calculation.⁹

Table S1. The fractions of free water, intermediate water, and bound water in the V-RGO foam with different compressive strains.

Compressive strain (%)	Free water fraction (%)	Intermediate water fraction (%)	Bound water fraction (%)	IW/FW ratio
0	72.04	26.70	1.26	0.37
11.8	67.40	29.71	2.89	0.44
23.5	58.89	38.31	2.8	0.65
35.3	56.65	39.84	3.51	0.70
47.1	51.62	42.09	6.29	0.82
52.9	53.46	40.98	5.56	0.77
58.9	62.72	34.65	2.63	0.55
61.8	69.87	28.73	1.4	0.41

Table S2. Comparison of the solar-thermal energy conversion performances of V-RGO foam with those reported in the literature.

Materials	Water Evaporation Rate (kg m⁻² h⁻¹)	Efficiency at 1 kW m⁻² (%)	Absorption (%)	Ref.
Double-layer cellulose-based hydrogel	1.582	91.4	94	12
RGO nanofluids	0.9	50	-	13
Wood@AIP	1.423	90.8	~98	14
MoS ₂ nanomaterials	1	68.1	96	15
Plasmonic absorber	2.7	79.3	92.9	16
ACF felt	1.22	79.4	94	17
Attapulgate/polyacrylamide	1.2	85	99	18
RGO hydrogel	2.4	~100	98	19
PVA/PPy hydrogel	3.2	94	~98	10
PVA/RGO hydrogel	2.5	85	~98	11
V-RGO hydrogel	3.39	104.1%	~97	This work

Table S3. The results of equivalent enthalpy and corresponding energy conversion efficiencies of V-RGO foams with different compressive strains.

Samples	Evaporation rate in a closed container (kg m ⁻² h ⁻¹)	Equivalent enthalpy (J g ⁻¹)	Conversion efficiency (%)
Water	0.0452	2444	21.7%
V-RGO-0%	0.0484	2283	92.6
V-RGO-11.8%	0.0558	2008	95.4
V-RGO-23.5%	0.0695	1614	100.4%
V-RGO-35.3%	0.0715	1579	101.8%
V-RGO-47.1%	0.0846	1306	104.1%
V-RGO-52.9%	0.0780	1435	102.9%
V-RGO-58.9%	0.0677	1653	98.3%
V-RGO-61.8%	0.0556	2012	97.3%

An experiment is designed to estimate the real vaporization enthalpy of water in the foam

An experiment is designed to estimate the real vaporization enthalpy of water in the foam, which is much lower than that of pure water. Water and the V-RGO foam (compressed by 47.1%) with the same surface area are placed in a sealed container with supersaturated potassium carbonate, which is used to stabilize the RH of ca. 45%, under a temperature of ca. 25°C, and an ambient air pressure. Since the input power is the same, the equivalent vaporization enthalpy of water can be calculated with eq. S8:¹⁰

$$U_{in} = \Delta H_0 m_0 = \Delta H_{equ} m_g \quad (S8)$$

Where U_{in} is input power, ΔH_0 and m_0 are the vaporization enthalpy and the mass change of bulk water, respectively; ΔH_{equ} and m_g are the equivalent vaporization enthalpy and the mass change of the foam, respectively. The vaporization enthalpy of water in the foam is about half of the vaporization enthalpy of pure water.

References

- Xu, N.; Hu, X.; Xu, W.; Li, X.; Zhou, L.; Zhu, S.; Zhu, J. Mushrooms as Efficient Solar Steam-Generation Devices. *Adv. Mater.* **2017**, *29*, 1606762.

2. Wang, H.; Zhang, R.; Yuan, D.; Xu, S.; Wang, L. Gas Foaming Guided Fabrication of 3D Porous Plasmonic Nanoplatfom with Broadband Absorption, Tunable Shape, Excellent Stability, and High Photothermal Efficiency for Solar Water Purification. *Adv. Funct. Mater.* **2020**, *30*, 2003995.
3. Wu, X.; Gao, T.; Han, C.; Xu, J.; Owens, G.; Xu, H. A Photothermal Reservoir for Highly Efficient Solar Steam Generation without Bulk Water. *Sci. Bull.* **2019**, *64*, 1625–1633.
4. Zhou, X.; Zhao, F.; Guo, Y.; Rosenberger, B.; Yu, G. Architecting Highly Hydratable Polymer Networks to Tune the Water State for Solar Water Purification. *Sci. Adv.* **2019**, *5*, eaaw5484.
5. Sun, Y.; Zhao, Z.; Zhao, G.; Wang, L.; Jia, D.; Yang, Y.; Liu, X.; Wang, X.; Qiu, J. High Performance Carbonized Corncob-Based 3D Solar Vapor Steam Generator Enhanced by Environmental Energy. *Carbon* **2021**, *179*, 337–347.
6. Guo, Y.; Lu, H.; Zhao, F.; Zhou, X.; Shi, W.; Yu, G. Biomass-Derived Hybrid Hydrogel Evaporators for Cost-Effective Solar Water Purification. *Adv. Mater.* **2020**, *32*, 1907061.
7. Guo, Y.; Lu, H.; Zhao, F.; Zhou, X.; Shi, W.; Yu, G. Biomass-Derived Hybrid Hydrogel Evaporators for Cost-Effective Solar Water Purification. *Adv. Mater.* **2020**, *32*, 1907061.
8. Martinez, L.; Andrade, R.; Birgin, E. G.; Martinez, J. M. Packmol: A Package for Building Initial Configurations for Molecular Dynamics Simulations. *J. Comput. Chem.* **2009**, *30*, 2157–2164.
9. Chen, X.; Jia, Y.; Sun, S.; Feng, L.; An, L. Performance Inhomogeneity of Gelatin During Gelation Process. *Polymer* **2009**, *50*, 6186-6191.
10. Zhao, F.; Zhou, X.; Shi, Y.; Qian, X.; Alexander, M.; Zhao, X.; Mendez, S.; Yang, R.; Qu, L.; Yu, G. Highly Efficient Solar Vapour Generation Via Hierarchically Nanostructured Gels. *Nat. Nanotechnol.* **2018**, *13*, 489–495.

11. Zhou, X.; Zhao, F.; Guo, Y.; Zhang, Y.; Yu, G. A Hydrogel-Based Antifouling Solar Evaporator for Highly Efficient Water Desalination. *Energy Environ. Sci.* **2018**, *11*, 1985–1992.
12. Hu, N.; Xu, Y.; Liu, Z.; Liu, M.; Shao, X.; Wang, J. Double-Layer Cellulose Hydrogel Solar Steam Generation for High-Efficiency Desalination. *Carbohydr. Polym.* **2020**, *243*, 116480.
13. Liu, X.; Wang, X.; Huang, J.; Cheng, G.; He, Y. Volumetric Solar Steam Generation Enhanced by Reduced Graphene Oxide Nanofluid. *Appl. Energy* **2018**, *220*, 302–312.
14. Chen, T.; Wu, Z.; Liu, Z.; Aladejana, J. T.; Wang, X. A.; Niu, M.; Wei, Q.; Xie, Y. Hierarchical Porous Aluminophosphate-Treated Wood for High-Efficiency Solar Steam Generation. *ACS Appl. Mater. Interfaces* **2020**, *12*, 19511–19518.
15. Wang, Q.; Qin, Y.; Jia, F.; Li, Y.; Song, S. Magnetic MoS_2 Nanosheets as Recyclable Solar-Absorbers for High-Performance Solar Steam Generation. *Renew. Energy* **2021**, *163*, 146–153.
16. Huang, Z.; Li, S.; Cui, X.; Wan, Y.; Xiao, Y.; Tian, S.; Wang, H.; Li, X.; Zhao, Q.; Lee, C.-S. A Broadband Aggregation-Independent Plasmonic Absorber for Highly Efficient Solar Steam Generation. *J. Mater. Chem. A* **2020**, *8*, 10742–10746.
17. Li, H.; He, Y.; Hu, Y.; Wang, X. Commercially Available Activated Carbon Fiber Felt Enables Efficient Solar Steam Generation. *ACS Appl. Mater. Interfaces* **2018**, *10*, 9362–9368.
18. Jia, J.; Liang, W.; Sun, H.; Zhu, Z.; Wang, C.; Li, A. Fabrication of Bilayered Attapulgite for Solar Steam Generation with High Conversion Efficiency. *Chem. Eng. J.* **2019**, *361*, 999–1006.
19. Liang, H.; Liao, Q.; Chen, N.; Liang, Y.; Lv, G.; Zhang, P.; Lu, B.; Qu, L. Thermal Efficiency of Solar Steam Generation Approaching 100% through Capillary Water Transport. *Angew. Chem. Int. Ed.* **2019**, *58*, 19041–19046.